Position estimation based on single pseudo-range measurements with unknown clock offset

Sara Barroso

***Abstract*—This paper addresses the problem of position estimation based on single pseudo-range measurements. An acoustic positioning system for an autonomous underwater vehicle (AUV) is considered. A one-way travel-time (OWTT) setting with an offset between the emitting and receiving clocks is assumed. Two cases are considered: one with known vehicle velocity and one where the velocity is only given in relation to the velocity of the surrounding fluid. Continuous-discrete filters are designed to obtain the desired estimates. In the first case, position and bias estimates are obtained with three different solutions: the extended Kalman filter (EKF), the unscented Kalman filter (UKF), and a linear Kalman filter (LKF) with an augmented state. The performances are assessed via simulation results and complemented by a thorough analysis with Monte Carlo simulations, which provide a comparison between the root mean square error (RMSE) of each of the three filters, and these with the Bayesian Crámer-Rao bound (BCRB). In the second case, position, velocity, and bias estimates are obtained. The chosen approach is to secure preliminary results through the use of the EKF, for which the performance is assessed via simulation results. The solution analysis is complemented with Monte Carlo simulations, which are carried out in order to compare the RMSE performance with the BCRB.**

***Index Terms*—underwater navigation; autonomous underwater vehicles; pseudo-range measurement; Kalman filter; augmented system**

I. Introduction

The use of AUVs has been increasing in recent years, with major applications in industrial, military [1], and research fields. Some notable missions are the mapping of the seafloor [2]; wreckage search for missing aircrafts [3] or ships; research applications, from the study of the ecosystems to the study of the evolution and predicted progressions of these bodies of water.

The question of localization of such vehicles is relevant whether for geo-referencing or control purposes. Traditional localization systems, such as the global positioning system (GPS), are not available in an underwater scenario due to the strong attenuation of the electromagnetic waves. Instead, a common choice is the use of acoustic transponders.

The three major categories of underwater acoustic positioning systems are the long baseline (LBL) [4], the short baseline (SBL) [5], and the ultra-short baseline (USBL) [6]–[8]. The USBL has smaller cost constraints but it also presents a lower accuracy. The LBL and SBL require a higher investment in equipment, since they involve the use of more acoustic transponders, as well as clock-synchronization software. The study of alternative localization methods, which can provide high accuracy in performance, while also maintaining a lower cost of production is, hence, imperative for the continued development of these types of missions.

In [9], the concept of a synthetic LBL (SLBL) is brought up. A single acoustic source is used, which is combined with a high performance dead-reckoning system to allow for the application of standard trilateration techniques. A similar idea is used in [10] with the definition of the virtual LBL (VLBL).

The EKF is a very widespread method used for solution estimation, namely in [11], [12]. In [13], conclusions are drawn about the boundedness of the estimation error of a discrete-time EKF, applied to a stochastic framework. These require specific conditions, including a sufficiently small initial error and sufficiently small noise, which are heavy constraints for navigation systems. For this reason, other approaches which provide global asymptotic stability are important in order to guarantee a more robust solution.

Some notable research on single range measurement positioning systems has been performed, namely in [14], where preliminary experimental results with single beacon acoustic navigation are presented. In [15], the problems of single range navigation and source localization are addressed. A solution based on an augmented state transforms the original nonlinear system into a linear time-varying (LTV) system, which enables the design of a LKF giving globally exponentially stable (GES) error dynamics. In [16], the observability of single range navigation is addressed, as well as some robustness issues.

The clock synchronization needed in a OWTT setting can be achieved prior to each mission via the appropriate calibrations. However, this is not only an added burden, but is also insufficient for long missions, since clock drift is inevitable unless clock synchronization is performed often. For this reason, solutions that can explicitly account for the bias term added by the clock offset, as in [17], are of great interest.

In [18], the author addresses both the single source and the clock offset concerns, previously mentioned in [15] and [17], respectively. Their combination yields estimations based on single pseudo-ranges. The solution presented includes deriving an augmented state, for which the system dynamics become linear and allow for the use of the LKF. This expands the previously obtained advantages, by solving both issues, while also obtaining GES guarantees. One of the main contributions of this paper is to expand upon the work in [18], by providing an extensive performance comparison between the proposed solution and other existing estimators, namely the EKF and the UKF. This is done through simulation results, along with Monte Carlo runs, including a comparison with the BCRB.

A. Notation

Throughout this paper, scalars, vectors, and matrices are represented by a lowercase letter, a bold lowercase letter,

and a bold uppercase letter, respectively. $\mathbf{I}_n$ denotes the $n\times n$ identity matrix. When matrix dimensions are omitted, the matrices are assumed to be of proper dimensions. A block diagonal matrix is represented by $\mathbf{diag}(\mathbf{A}_1,...,\mathbf{A}_n)$. For $\mathbf{x}\in\mathbb{R}^3$, x_x, x_y and x_z represent the x, y and z axis components of $\mathbf{x}$, respectively. The transpose operator is denoted by $(.)^T$. The Special Orthogonal Group is denoted by $\mathrm{SO}(3)=\{\mathbf{X}\in\mathbb{R}^{3\times3}:\mathbf{X}\mathbf{X}^T=\mathbf{X}^T\mathbf{X}=\mathbf{I}_3\wedge\det(\mathbf{X})=1\}$.

II. Problem statement

Consider an acoustic positioning system for an underwater vehicle, consisting of a fixed emitting source. The agent is equipped with an acoustic receiver and is assumed to have access to the inertial position of the emitter, which is constant. A OWTT setting is considered, with no guarantee of clock synchronization between source and agent. This time offset results in a bias term in the range measurements, which are, then, pseudo-range measurements, obtained with sampling period T. The vehicle is equipped with an attitude and heading reference system (AHRS) and a Doppler velocity log (DVL), to obtain the necessary additional information about its movement.

Due to the associated sampling rates, the nonlinear system dynamics derived in the following sections are considered in a continuous-discrete framework and then discretized. This makes the pseudo-range measurements, obtained at low update rates, drive the estimation error to zero, while the other sensors, which operate at a higher rate, are used to drive the system dynamics.

Let $\{I\}$ denote the local inertial coordinate reference frame and $\{B\}$ denote the coordinate frame attached to the vehicle, usually referred to as the body-fixed reference frame. Considering $\mathbf{p}(t)\in\mathbb{R}^3$ as the inertial position of the vehicle, $\mathbf{v}(t)\in\mathbb{R}^3$ as the velocity of the vehicle relative to $\{I\}$, expressed in body-fixed coordinates, and $\mathbf{R}(t)\in\mathrm{SO}(3)$ as the rotation matrix from $\{B\}$ to $\{I\}$, given by the AHRS, the linear motion of the vehicle is, then, described by

$$\dot{\mathbf{p}}(t)=\mathbf{R}(t)\mathbf{v}(t). \tag{1}$$

In this work, two scenarios will be considered: one in which it is assumed that the bottom-lock condition is verified, and so, the inertial velocity values are directly available to the vehicle, and one which corresponds to the absence of bottom-lock, where only the velocity of the vehicle relative to the fluid is available. The inertial position of the source, which is assumed to be fixed, is denoted by $\mathbf{s}\in\mathbb{R}^3$. Let $b_c(t_k)$ be the bias term that accounts for the effect of the unknown clock offset. The pseudo-range measurements available to the vehicle are then given by

$$r(k)=\|\mathbf{s}-\mathbf{p}(t_k)\|+b_c(t_k), \tag{2}$$

with $t_k=t_0+kT, k\in\mathbb{N}$, where $T>0$ is the sampling period and t_0 is the initial time.

Assumption 1. All the pseudo-range measurements are positive, i.e., $r(k)>0$ for all k.

Remark 1. The condition in Assumption 1 is a mild one. Indeed, if the vehicle were to receive a signal in which the time tag was greater than its own clock, it would know that its clock is behind and could adjust its value to a higher one, so that the pseudo-range measurement is positive.

Assumption 2. The offset of the clocks is constant, i.e., $\dot{b}_c(t)=0$.

Remark 2. The presented solutions are designed to be noise controllable, i.e. the noise covariance matrices do not have zero diagonal values. This means that, even though the bias term is assumed constant, in nominal terms, it is possible to track slow time-varying quantities.

A. System dynamics with bottom-lock

Considering the scenario in which bottom-lock can be guaranteed, i.e., the vehicle has direct access to the inertial velocity values, the system can be described by a continuous nonlinear system with discrete-time output, which is obtained by combining the previous assumptions with (1) and (2), giving

$$\begin{cases}\dot{\mathbf{p}}(t)=\mathbf{R}(t)\mathbf{v}(t)\\ \dot{b}_c(t)=0\\ r(k)=\|\mathbf{s}-\mathbf{p}(t_k)\|+b_c(t_k)\end{cases}. \tag{3}$$

By discretizing system (3), the discrete-time system dynamics can be described by

$$\begin{cases}\mathbf{p}(t_{k+1})=\mathbf{p}(t_k)+\int_{t_k}^{t_{k+1}}\mathbf{R}(\tau)\mathbf{v}(\tau)d\tau\\ b_c(t_{k+1})=b_c(t_k)\\ r(k)=\|\mathbf{s}-\mathbf{p}(t_k)\|+b_c(t_k)\end{cases}. \tag{4}$$

Using the system described in (4) and defining the discrete-time states

$$\begin{cases}\mathbf{x}_1(k)=\mathbf{p}(t_k)\\ x_2(k)=b_c(t_k)\end{cases},$$

one can write

$$\begin{cases}\mathbf{x}_1(k+1)=\mathbf{x}_1(k)+\mathbf{u}(k)\\ x_2(k+1)=x_2(k)\end{cases},$$

with $\mathbf{u}(k)=\int_{t_k}^{t_{k+1}}\mathbf{R}(\tau)\mathbf{v}(\tau)d\tau$. From here, it is possible to rewrite the system dynamics as

$$\begin{cases}\mathbf{x}(k+1)=\mathbf{A}\mathbf{x}(k)+\mathbf{B}\mathbf{u}(k)\\ r(k)=\|\mathbf{s}-\mathbf{x}_1(k)\|+x_2(k)\end{cases}, \tag{5}$$

where $r(k)$ are the pseudo-range measurements available to the vehicle. The state and input matrices, respectively $\mathbf{A}=\mathbf{I}_4$ and $\mathbf{B}=\mathbf{diag}(\mathbf{I}_3,0)$, are constant over time.

B. System dynamics without bottom-lock

In the absence of bottom-lock, the DVL provides only the velocity of the vehicle relative to the velocity of its surrounding fluid. In (1), $\mathbf{v}(t)$ is, thus, the sum of its two components. Let $\mathbf{v}_f(t)\in\mathbb{R}^3$ denote the velocity of the fluid in inertial coordinates and $\mathbf{v}_r(t)\in\mathbb{R}^3$ denote the velocity of the vehicle relative to the fluid in body-fixed coordinates. Hence,

$$\mathbf{v}(t)=\mathbf{R}^T(t)\mathbf{v}_f(t)+\mathbf{v}_r(t). \tag{6}$$

Assumption 3. The inertial fluid velocity is constant, i.e., $\dot{\mathbf{v}}_f(t)=\mathbf{0}_{3\times1}$.

Remark 3. Once again, using the argument of noise controllability, this restriction can be loosened and it is possible to track slow time-varying quantities.

With all three assumptions and combining (1), (2), and (6) gives the continuous non-linear system with discrete-time output

$$\begin{cases}\dot{\mathbf{p}}(t)=\mathbf{v}_f(t)+\mathbf{R}(t)\mathbf{v}_r(t)\\ \dot{\mathbf{v}}_f(t)=0\\ \dot{b}_c(t)=0\\ r(k)=\|\mathbf{s}-\mathbf{p}(t_k)\|+b_c(t_k)\end{cases}. \tag{7}$$

By discretizing system (7), the discrete-time system dynamics can be described by

$$\begin{cases}\mathbf{p}(t_{k+1})=\mathbf{p}(t_k)+T\mathbf{v}_f(t_k)+\int_{t_k}^{t_{k+1}}\mathbf{R}(\tau)\mathbf{v}_r(\tau)d\tau\\ \mathbf{v}_f(t_{k+1})=\mathbf{v}_f(t_k)\\ b_c(t_{k+1})=b_c(t_k)\\ r(k)=\|\mathbf{s}-\mathbf{p}(t_k)\|+b_c(t_k)\end{cases}. \tag{8}$$

Using the system described in (8) and defining the discrete-time states

$$\begin{cases}\mathbf{x}_1(k)=\mathbf{p}(t_k)\\ \mathbf{x}_2(k)=\mathbf{v}_f(t_k)\\ x_3(k)=b_c(t_k)\end{cases},$$

one can write

$$\begin{cases}\mathbf{x}_1(k+1)=\mathbf{x}_1(k)+T\mathbf{x}_2(k)+\mathbf{u}(k)\\ \mathbf{x}_2(k+1)=\mathbf{x}_2(k)\\ x_3(k+1)=x_3(k)\end{cases},$$

with $\mathbf{u}(k)=\int_{t_k}^{t_{k+1}}\mathbf{R}(\tau)\mathbf{v}_r(\tau)d\tau$. From here, it is possible to rewrite the system dynamics as

$$\begin{cases}\mathbf{x}(k+1)=\mathbf{A}\mathbf{x}(k)+\mathbf{B}\mathbf{u}(k)\\ r(k)=\|\mathbf{s}-\mathbf{x}_1(k)\|+x_3(k)\end{cases}, \tag{9}$$

where $r(k)$ are the pseudo-range measurements available to the vehicle. The state and input matrices, respectively $\mathbf{A}$ and $\mathbf{B}$, are constant over time, as given by

$$\mathbf{A}=\begin{bmatrix}1&0&0&T&0&0&0\\0&1&0&0&T&0&0\\0&0&1&0&0&T&0\\0&0&0&1&0&0&0\\0&0&0&0&1&0&0\\0&0&0&0&0&1&0\\0&0&0&0&0&0&1\end{bmatrix}\quad\text{and}\quad\mathbf{B}=\begin{bmatrix}1&0&0\\0&1&0\\0&0&1\\0&0&0\\0&0&0\\0&0&0\\0&0&0\end{bmatrix}. \tag{10}$$

III. Simulation Results

In the simulations, the vehicle describes the trajectory depicted in Fig. 1. Its initial position is $\mathbf{p}=\begin{bmatrix}1&1&1\end{bmatrix}$ [m], whereas the constant bias value is $b_c=2$m. The fixed position of the source is $\mathbf{s}=\begin{bmatrix}1&1&3\end{bmatrix}$ [m].

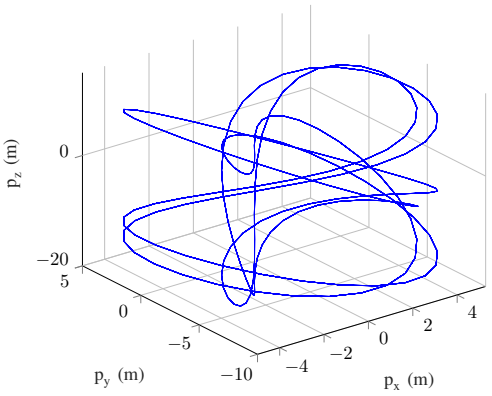

Fig. 1: Trajectory described by the vehicle.

A. Simulation results for system with bottom-lock

The problem of estimator design for (5) is approached by designing an EKF, an UKF, and a LKF with state augmentation. The state augmentation follows the one introduced in [18], where the author takes advantage of the fact that the only nonlinearity in this problem comes from the system range measurements. Because these values are measured at each timestamp, and hence, are accessible to the state, it is possible to define

$$\begin{cases}\mathbf{z}_1(k)=\mathbf{x}_1(k)\\ z_2(k)=x_2(k)\\ z_3(k)=r(k)\end{cases},$$

where $r(k)=\|\mathbf{x}_1(k)\|+x_2(k)$, which yields the new state vector $\mathbf{z}(k)=\begin{bmatrix}\mathbf{z}_1^T(k)&z_2(k)&z_3(k)\end{bmatrix}^T$. Noticing that

$$\begin{cases}\mathbf{z}_1(k+1)=\mathbf{z}_1(k)+\mathbf{u}(k)\\ z_2(k+1)=z_2(k)\\ z_3(k+1)=\|\mathbf{z}_1(k+1)\|+z_2(k+1)\end{cases}$$

one can arrive at the new state-space formulation

$$\begin{cases}\mathbf{z}(k+1)=\mathbf{A}(k)\mathbf{z}(k)+\mathbf{B}(k)\mathbf{u}(k)\\ y(k+1)=\mathbf{C}\mathbf{z}(k+1)\end{cases}. \tag{11}$$

The new state, input, and output matrices are given by

$$\mathbf{A}(k)=\begin{bmatrix}\mathbf{I}_3&\mathbf{0}_{3\times1}&\mathbf{0}_{3\times1}\\ \mathbf{0}_{1\times3}&1&0\\ 2\dfrac{\mathbf{u}(k)^T}{r(k+1)}&2\dfrac{[r(k+1)-r(k)]}{r(k+1)}&\dfrac{r(k)}{r(k+1)}\end{bmatrix}\in\mathbb{R}^{5\times5},$$

$$\mathbf{B}(k)=\begin{bmatrix}\mathbf{I}_3\\ \mathbf{0}_{1\times3}\\ \dfrac{\mathbf{u}(k)^T}{r(k+1)}\end{bmatrix}\in\mathbb{R}^{5\times3},$$

and $\mathbf{C}=\begin{bmatrix}\mathbf{0}_{1\times3}&0&1\end{bmatrix}\in\mathbb{R}^{1\times5}$, respectively. The input is still $\mathbf{u}(k)=\int_{t_k}^{t_{k+1}}\mathbf{R}(\tau)\mathbf{v}_r(\tau)d\tau$. The new system can be regarded as a discrete-time linear time-varying for observer design purposes. Since the augmented system is equivalent to the system in (5), an observer (filter) for (11) is also an observer (filter) for (5).

The proposed observers are simulated considering sensor noise for all sensors. The pseudo-range measurements are assumed to be subjected to additive zero-mean Gaussian noise with standard deviation $0.1\mathrm{m}$, whereas the process noise is considered to be additive zero-mean Gaussian noise with standard deviation $1\mathrm{cm}$. To evaluate the robustness of the solutions, a non-zero initial error is considered. The EKF and the UKF are initialized with $\mathbf{P}(0)=\mathbf{I}_4$ and $\mathbf{x}(0)=\begin{bmatrix}-4 & -4 & -4 & 1\end{bmatrix}^T[\mathrm{m}]$, whereas the LKF is initialized with $\mathbf{P}(0)=\mathbf{I}_5$ and $\mathbf{z}(0)=\begin{bmatrix}-4 & -4 & -4 & 1 & r(0)\end{bmatrix}^T[\mathrm{m}]$ due to the augmented state.

The initial convergence of the position estimation error is depicted in Figures 2, 3, and 4, respectively for the EKF, the UKF, and the LKF. The initial convergence of the bias estimation error for each filter is presented in Fig. 5. One can immediately see an underperformance of the UKF, as it presents the highest convergence time. The LKF clearly presents the fastest convergence, as well as the smallest initial transients.

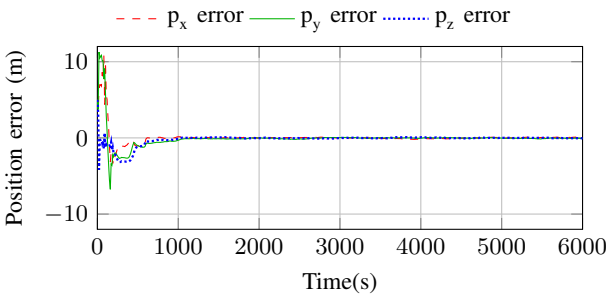

Fig. 2: EKF initial convergence of the position estimation errors.

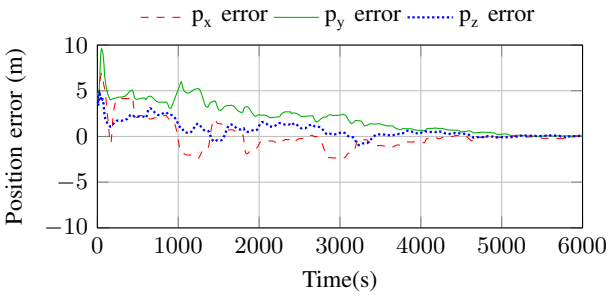

Fig. 3: UKF initial convergence of the position estimation errors.

Because the three components of the position show similar behaviours, the detailed evolution of the position p_x estimation error is shown in Fig. 6 and is considered representative of all components. The detailed evolution of the bias estimation error is presented in Fig. 7. Both evolutions seem to indicate similar steady-state estimation errors for all filters.

1) Filter failure of convergence: Since neither the EKF nor the UKF provide convergence guarantees, an example of a set of initial conditions for which the filters do not converge is presented. For the EKF, a simulation is run with $\mathbf{P}(0)=\mathbf{I}_4$ and $\mathbf{z}(0)=\begin{bmatrix}-999 & -699 & -999 & -498\end{bmatrix}^T[\mathrm{m}]$. Figures 8 and 9 show

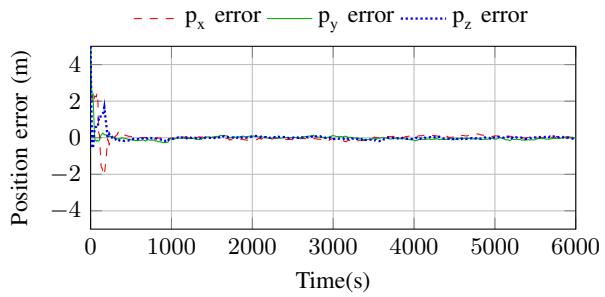

Fig. 4: LKF initial convergence of the position estimation errors.

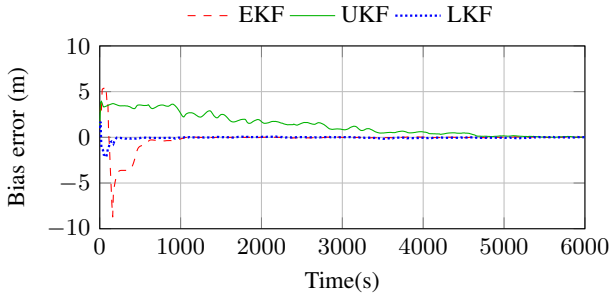

Fig. 5: Initial convergence of the bias estimation error.

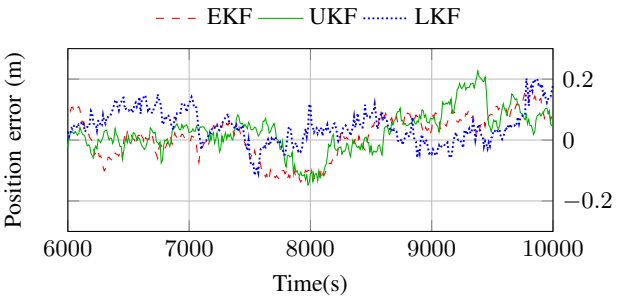

Fig. 6: Detailed evolution of the position p_x estimation error.

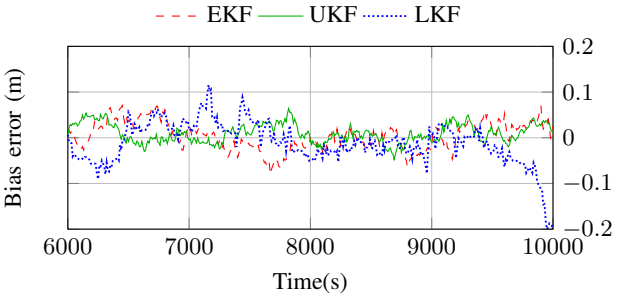

Fig. 7: Detailed evolution of the bias estimation error.

the obtained position and bias estimation errors, respectively. These prove that the filter does not converge under these conditions.

The LKF is run with equivalent conditions, i.e., with $\mathbf{P}(0)=\mathbf{I}_5$ and $\mathbf{x}(0)=\begin{bmatrix}-999 & -699 & -999 & -498 & r(0)\end{bmatrix}^T[\mathrm{m}]$. Figures 10 and 11 show the initial convergence and steady-state results obtained for the position estimation error and bias estimation error, respectively. These results illustrate the benefits of using

the solution proposed in [18], since it provides GES, which means it will converge even when equivalent filters do not.

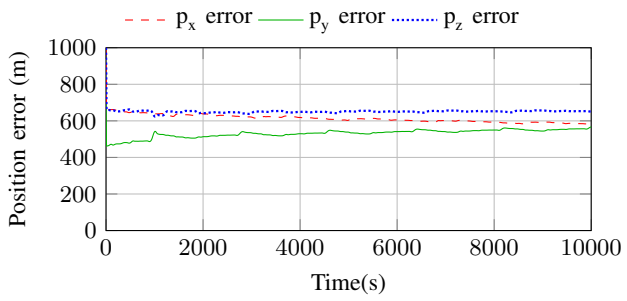

Fig. 8: EKF failure of convergence: position error.

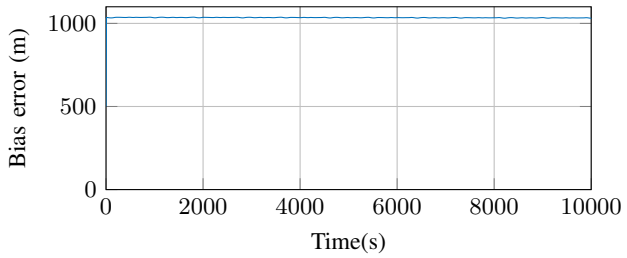

Fig. 9: EKF failure of convergence: bias error.

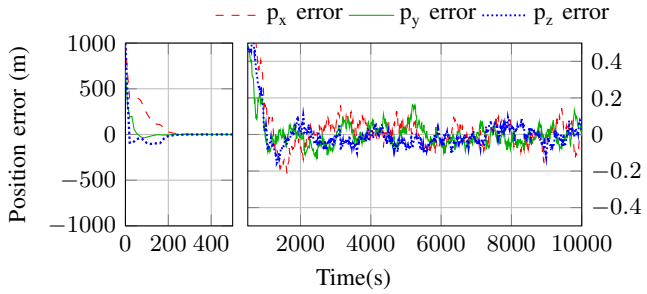

Fig. 10: LKF convergence for an initial condition that leads to failure of the EKF: position error.

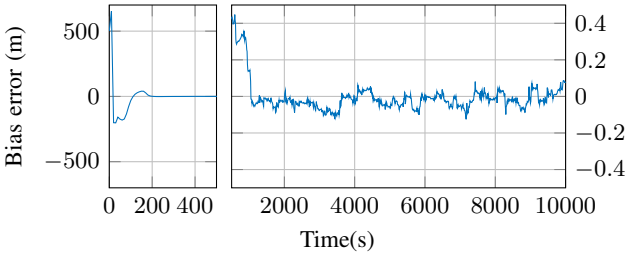

Fig. 11: LKF convergence for an initial condition that leads to failure of the EKF: bias error.

For the UKF, a simulation is run with $\mathbf{P}(0)=\mathbf{I}_4$ and $\mathbf{x}(0)=\begin{bmatrix}-24 & -14 & -24 & -2\end{bmatrix}^T$ [m]. Figures 12 and 13 show the obtained position and bias estimation errors, respectively. These prove that the filter does not converge under these conditions. Notice that the necessary offset needed for UKF failure of convergence is much smaller than the one used in the equivalent EKF experiment.

The LKF is run with equivalent conditions, i.e., with $\mathbf{P}(0)=\mathbf{I}_5$ and $\mathbf{x}(0)=\begin{bmatrix}-24 & -14 & -24 & -2 & r(0)\end{bmatrix}^T$ [m]. Figures 14 and 15 show the initial convergence and steady-state results obtained for the position estimation error and bias estimation error, respectively. These results further support the benefits of the GES guarantee of this solution.

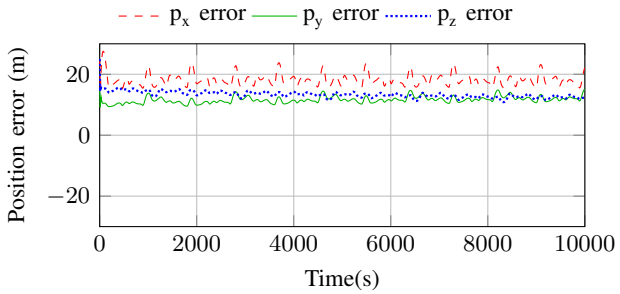

Fig. 12: UKF failure of convergence: position error.

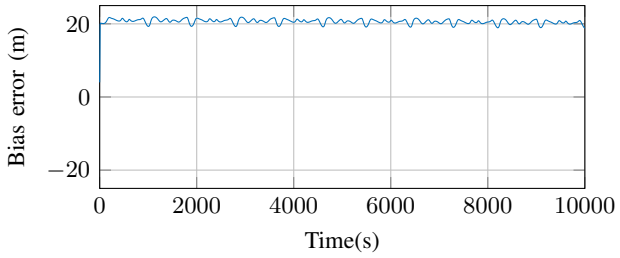

Fig. 13: UKF failure of convergence: bias error.

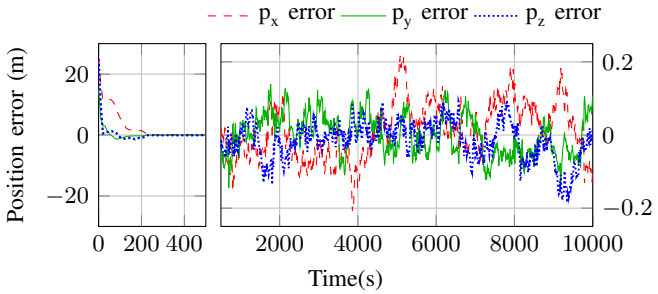

Fig. 14: LKF convergence for an initial condition that leads to failure of the UKF: position error.

2) Monte Carlo runs for system with bottom-lock: In order to characterize the performances of the proposed solutions, the Monte Carlo method is applied. 10000 runs are carried out for the scenario described in Section III-A. The same noise covariance matrices are used. The offset added to the nominal initial conditions in order to obtain the non-zero initial error is sampled from a zero-mean Gaussian distribution with covariance matrix $\mathbf{P}=\mathbf{diag}(100\mathbf{I}_3,25)$, which is also the initial covariance matrix of the filters. For the LKF this becomes $\mathbf{P}=\mathbf{diag}(100\mathbf{I}_3,25,10^{-4})$.

Table I presents some outcomes of the Monte Carlo simulations. It is clear that the UKF has the longest run time and that

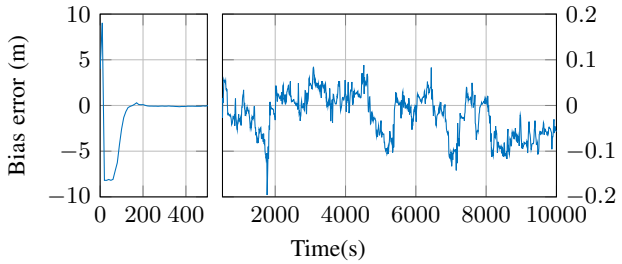

Fig. 15: LKF convergence for an initial condition that leads to failure of the UKF: bias error.

the EKF has the lowest final average errors for all variables. Regarding the LKF it is important to note that the only run that is not counted as a convergence is not a case of failure of convergence, but a case in which the final error did not fall under the established thresholds for convergence.

TABLE I: Monte Carlo outcomes for system with bottom-lock.

Filter	Number of runs that converge	Run time (min)	Final average position error (cm)	Final average bias error (m)
EKF	10000	4.55	$[-0.022\,0.079\,-0.046]^T$	8.21×10^{-4}
UKF	8278	17.45	$[-1.69\,4.26\,0.67]^T$	0.023
LKF	9999	6.03	$[0.487\,-0.470\,-0.632]^T$	-0.016

The initial convergence of the average position estimation error is depicted in Figures 16, 17, and 18, respectively for the EKF, UKF, and LKF. Fig. 19 presents the average bias estimation error for each filter and shows a longer convergence time and higher peaks for the UKF. Because the three components of the position show similar behaviours, only the detailed evolution of the position p_x is shown in Fig. 20 without loss of information. The detailed evolution of the bias is presented in Fig. 21 and seems to indicate a slight offset in the LKF bias estimation. These detailed evolutions once again demonstrate the significantly worse performance of the UKF in comparison with the other two filters.

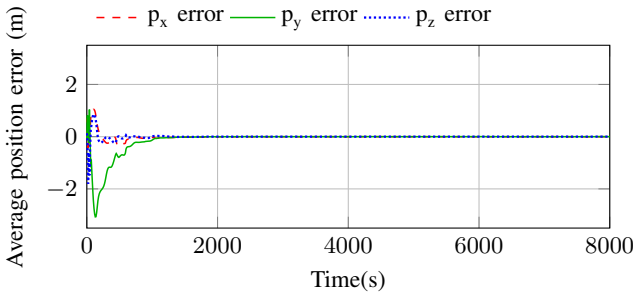

Fig. 16: EKF initial convergence of the average position estimation errors.

Fig. 22 shows the initial convergence of the RMSE of the position p_x, which again is representative of the behaviour of the remaining components of the position. This shows the results of all three estimators and allows for a direct comparison of performance between the filters, and with the theoretical performance limit, given by the BCRB. Fig 23

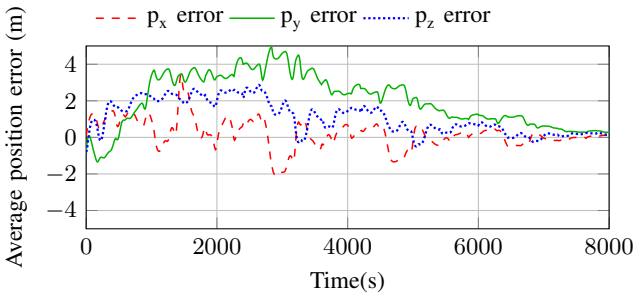

Fig. 17: UKF initial convergence of the average position estimation errors.

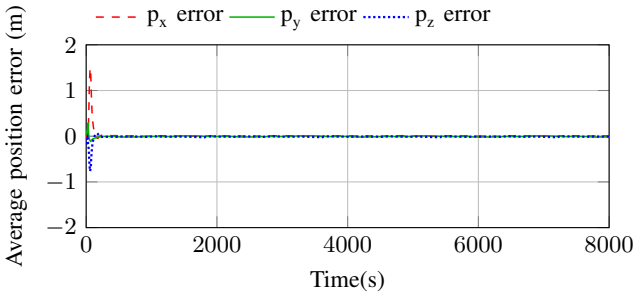

Fig. 18: LKF initial convergence of the average position estimation errors.

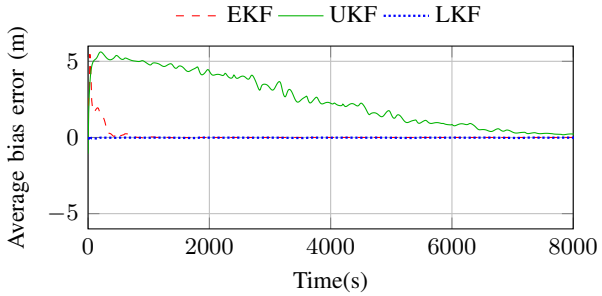

Fig. 19: Initial convergence of the average bias estimation error.

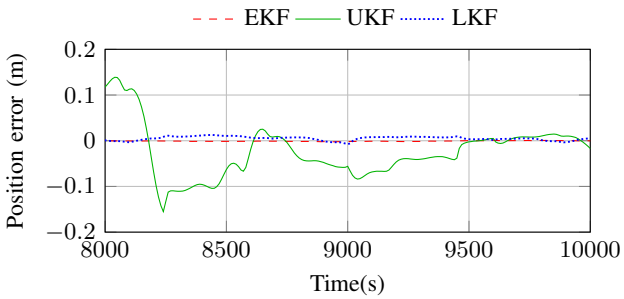

Fig. 20: Detailed evolution of the average position p_x estimation error.

presents the initial convergence of the bias RMSE for all filters and for the BCRB. One can notice a relatively high peak in the initial transient of the EKF.

Fig. 24 depicts the detailed evolution of the RMSE of the position p_x. One can obtain some further insight regarding

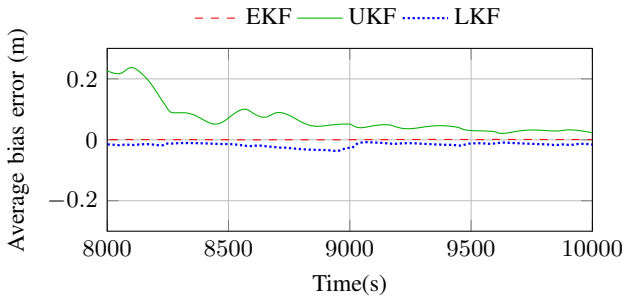

Fig. 21: Detailed evolution of the average bias estimation error.

previous experiments by noticing that the UKF presents the largest difference from the BCRB. The LKF does not seem to be an optimal estimator for the problem at hand, since its tracking of the BCRB is not overlapping, although it is clearly a much better solution than the UKF. The EKF presents the smallest difference from the BCRB which might, at first glance, make it seem like the better solution. However, one should notice the points at which the EKF RMSE falls below the BCRB line, which seems to indicate a somewhat biased estimation for this variable.

Fig. 25 presents the detailed evolution of the bias RMSE. Like for the position, the UKF bias RMSE is clearly the worse performing of the three solutions. The hypothesis from before regarding a possible offset in the bias estimation is now clear, as both the EKF and the LKF fall below the BCRB line. It is also clear, from Figures 24 and 25, that the EKF is the most biased of these two estimators.

Table II presents the numerical results obtained for the average RMSE between 5000 s and 10000 s for each filter, as well as the average BCRB value in the same interval. These once again show the poorer results achieved by the UKF and indicate that the EKF slightly outperforms the LKF in terms of the steady-state values.

TABLE II: Average RMSE and BCRB values between 5000 s and 10000 s.

	p_x(m)	p_y(m)	p_z(m)	b_c(m)
BCRB	0.0678	0.0570	0.0478	0.0421
RMSE EKF	0.0656	0.0551	0.0441	0.0296
RMSE UKF	0.9525	0.9005	0.4022	0.6831
RMSE LKF	0.0742	0.0647	0.0520	0.0483

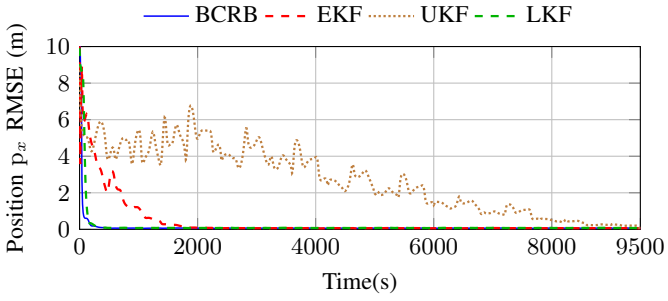

Fig. 22: Initial convergence of the position p_x RMSE.

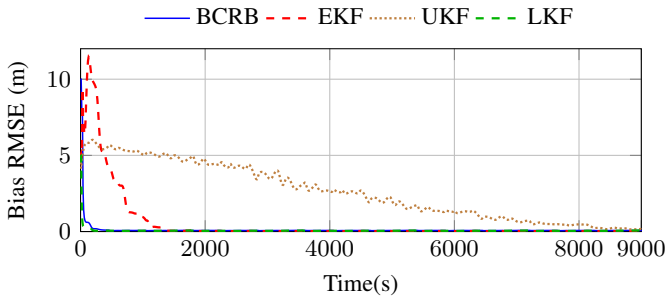

Fig. 23: Initial convergence of the bias RMSE.

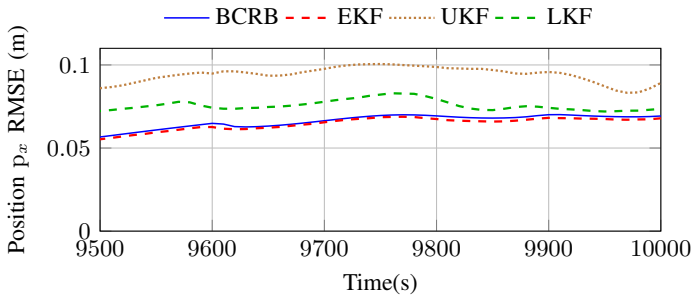

Fig. 24: Detailed evolution of the position p_x RMSE.

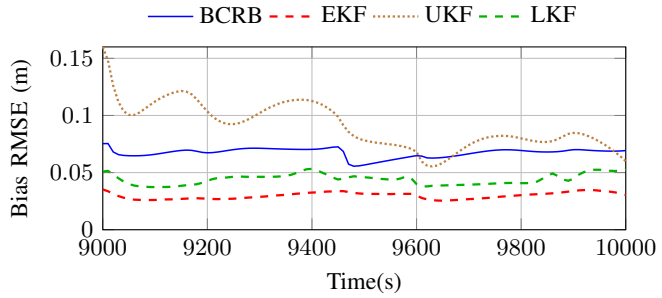

Fig. 25: Detailed evolution of the bias RMSE.

B. Simulation results for system without bottom-lock

In addition to the initial position, bias, and source position values, $\mathbf{p}(0)=\begin{bmatrix}1 & 1 & 1\end{bmatrix}$ [m], $b_c=2$m, and $\mathbf{s}=\begin{bmatrix}1 & 1 & 3\end{bmatrix}$ [m], respectively, the system now considers a velocity. $\mathbf{v}_f(t)$ is considered, for simulation purposes, to simply be the compensation of the fluid velocity, so that the described trajectory is still the one depicted in Fig. 1. This constant velocity is given by $\mathbf{v}_f(t)=[0.1\,0.1\,0.1]^T$[m/s].

The proposed solution is simulated considering sensor noise for all sensors. The pseudo-range measurements are assumed to be subjected to additive zero-mean Gaussian noise with standard deviation 1cm, whereas the process noise is considered to be additive zero-mean Gaussian noise with covariance matrix $\mathbf{Q}=\mathbf{diag}(10^{-4}\mathbf{I}_3, 10^{-6}\mathbf{I}_4)$. To evaluate the robustness of the solutions, a non-zero initial error is considered. The EKF is initialized with $\mathbf{P}(0)=\mathbf{I}_7$ and $\mathbf{x}_1(0)=\begin{bmatrix}0 & 0 & 0\end{bmatrix}^T$ [m], $\mathbf{x}_2(0)=\begin{bmatrix}0.03 & 0.03 & 0.03\end{bmatrix}^T$ [m/s], and $x_3=1.7$m.

The initial convergence of the estimation errors for this filter is depicted in Figures 26, 27, and 28, respectively for the position, velocity, and bias errors. The detailed evolution of these errors in shown in Figures 29, 30, and 31, in the

same order. These show a much slower convergence than its equivalent experiment with bottom-lock, which is to be expected due to the increased difficulty of an already hard problem. Even though Fig. 31 shows an offset in the final bias estimation error, all detailed evolutions show the estimation errors growing closer to zero for larger time-stamps, with very satisfactory steady-state errors, considering the scale of the problem.

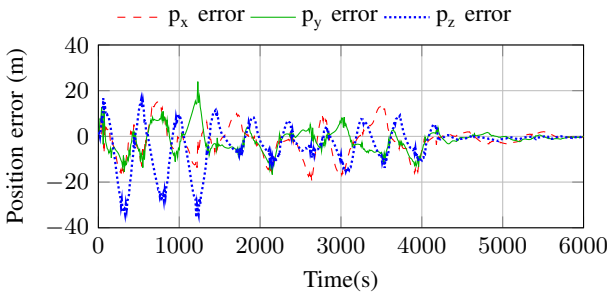

Fig. 26: EKF without bottom-lock initial convergence of the position estimation errors.

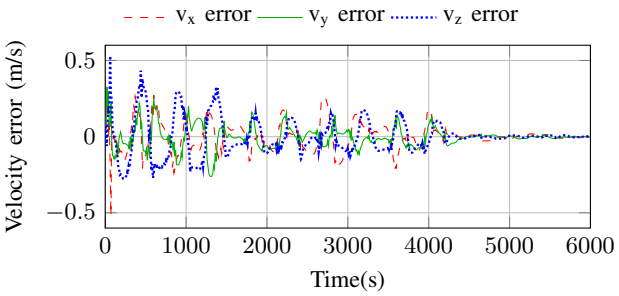

Fig. 27: EKF without bottom-lock initial convergence of the velocity estimation errors.

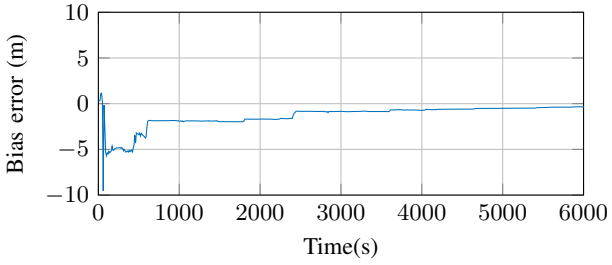

Fig. 28: EKF without bottom-lock initial convergence of the bias estimation error.

1) Filter failure of convergence: Even though satisfactory results are achieved, this is only a primary approach to this problem and future work should be performed in order to provide a solution with asymptotic stability. A set of initial estimates for which the designed filter does not converge is given by $\mathbf{x}_1(0) = \begin{bmatrix} -4999 & -3999 & -4999 \end{bmatrix}^T [\mathrm{m}]$, $\mathbf{x}_2(0) = \begin{bmatrix} -1.9 & -0.9 & -1.9 \end{bmatrix}^T [\mathrm{m/s}]$, and $\mathrm{x}_3(0) = -4498 \mathrm{m}$. Figures 32, 33, and 34 depict the obtained results for the position,

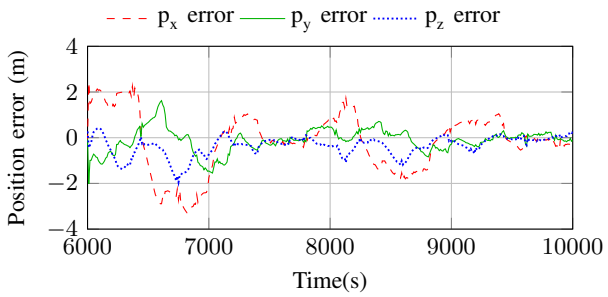

Fig. 29: EKF without bottom-lock detailed evolution of the position p_x estimation error.

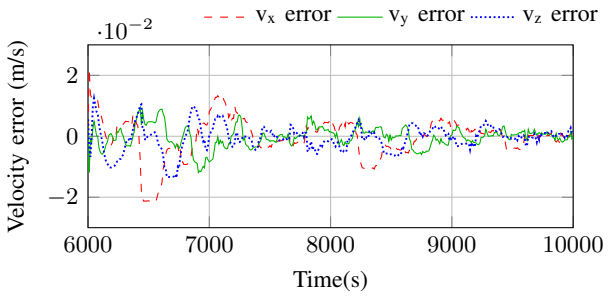

Fig. 30: EKF without bottom-lock detailed evolution of the velocity v_x estimation error.

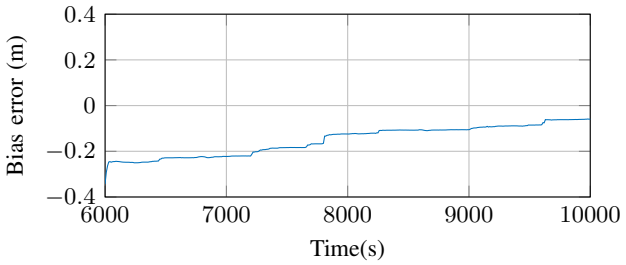

Fig. 31: EKF without bottom-lock detailed evolution of the bias estimation error.

velocity, and bias errors, respectively. All three plots clearly show a failure of convergence of the designed filter.

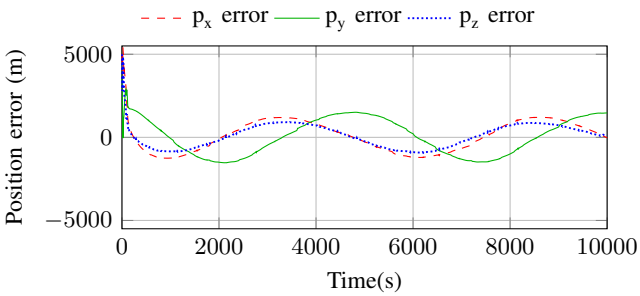

Fig. 32: Example of failure of convergence of the EKF without bottom-lock: position error.

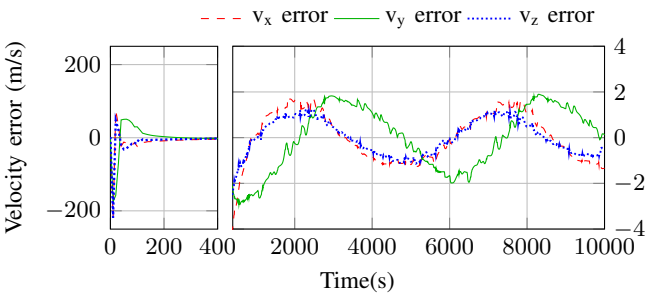

Fig. 33: Example of failure of convergence of the EKF without bottom-lock: velocity error.

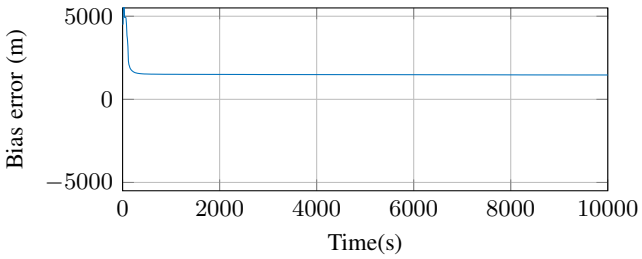

Fig. 34: Example of failure of convergence of the EKF without bottom-lock: bias error.

2) Monte Carlo runs for system without bottom-lock: In order to characterize the performances of the proposed solutions, the Monte Carlo method is applied. 10000 runs are carried out for the scenario described in Section III-B. The same noise covariance matrices are used. The offset added to the nominal initial conditions in order to obtain the non-zero initial error is sampled from a zero-mean Gaussian distribution with covariance matrix $\mathbf{P}=\mathbf{diag}(100\mathbf{I}_3,0.01\mathbf{I}_3,25)$, which is also the initial covariance matrix of the filter.

Once again, without loss of information, p_x is chosen to represent all three position components and v_x represents the velocity components. The average estimation errors for the EKF without bottom-lock are depicted in Figures 35, 36, and 37, respectively for position p_x, velocity v_x, and the bias. These show longer convergence times when compared to the equivalent figures for the EKF with bottom-lock. The bias achieves the same order of magnitude shown in Fig. 21, however the position presents a much higher average error. Taking into account the increased difficulty of this estimation, as well as the scale of the problem, one can still attest to the good performance of the filter.

Since this type of filter tends to overestimate its performance, it is interesting to compare its perception with the actual results. For this reason, the RMSE is compared against the BCRB, like before, but also against the standard deviation obtained from the filter. This is done by taking the square root of the diagonal entries of the covariance matrix $\mathbf{P}$. The RMSE of the position p_x is depicted in Fig. 38 and shows some indication that the filter might become biased for longer experiments, since its internal perception consistently falls below the BCRB line. The RMSE of velocity v_x is presented in Fig. 39. The bias RMSE is depicted in Fig. 40. All three figures show a RMSE that is considerably above the BCRB

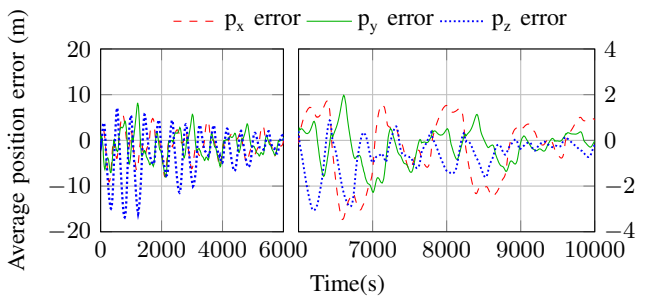

Fig. 35: EKF without bottom-lock average position estimation error.

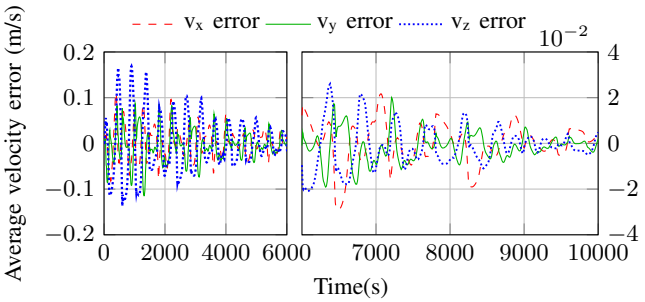

Fig. 36: EKF without bottom-lock average velocity estimation error.

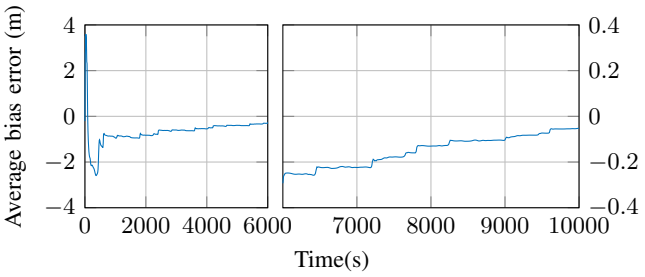

Fig. 37: EKF without bottom-lock average bias estimation error.

which justifies the higher difficulty in convergence previously mentioned.

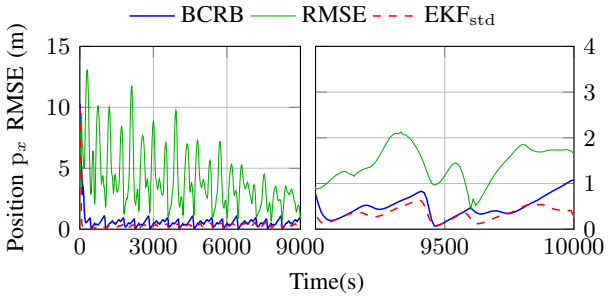

Fig. 38: EKF without bottom-lock position p_x RMSE.

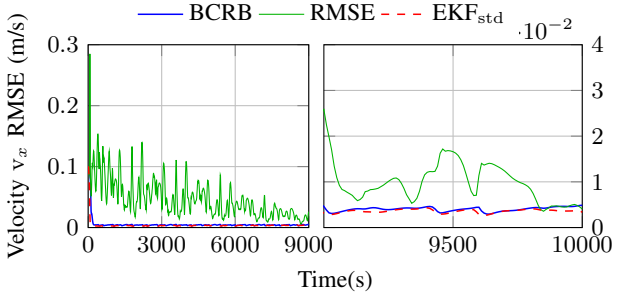

Fig. 39: EKF without bottom-lock velocity v_x RMSE.

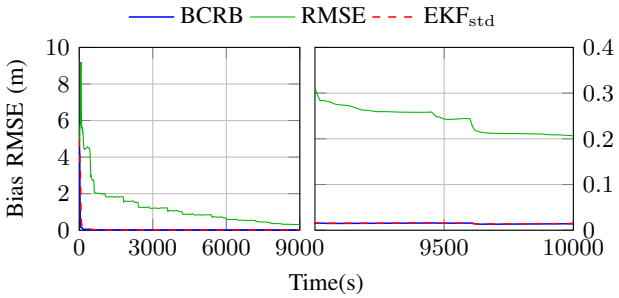

Fig. 40: EKF without bottom-lock bias RMSE.

IV. Conclusions and Future Work

The work developed in this paper addressed two problems of localization based on single pseudo-range measurements. For the system with bottom-lock, the three position components, as well as the bias associated with the clock offset, were successfully estimated. The three proposed solutions for this problem were compared, via simulation results, under the same conditions. A thorough Monte Carlo analysis was performed, for which the RMSE and average error of the solutions were computed and compared. Initial conditions for which the EKF and the UKF do not converge were shown. Equivalent simulations were performed with the LKF, which proved to converge in both cases due to its GES guarantee. Overall, the UKF is clearly the worst performing filter for this estimation, with worse obtained estimates, slowest convergence and highest run time. Because the EKF and LKF present comparable results, as well as computational costs, and since the LKF shows a much faster convergence, although a slightly higher steady-state error than the EKF, the global convergence guarantee of the LKF forces the conclusion that the LKF is the best estimator solution out of the ones analysed.

For the system without bottom-lock, only an introductory approach was taken, with the design and testing of an EKF. The three position components, the three velocity components, and the bias associated with the clock offset were successfully estimated. This filter presented a much longer convergence time when compared with the version with bottom-lock, which is to be expected considering the increased difficulty of the problem. The resulting steady-state errors were also higher than before, as well as the difference between the obtained RMSE and the BCRB for this system. However, because the results are still deemed satisfactory, and a convergence within the set thresholds is obtained for most Monte Carlo runs, this is still a good estimator.

Future work can be done for the system without bottom-lock by taking a similar approach and designing a LKF by further augmenting the state. The same analysis performed in this work for the system with bottom-lock should be carried out for the system without bottom-lock, by performing an extensive comparison between the EKF and LKF. A comparison with the UKF could also be attempted, although, given the results obtained in this paper, it is unlikely that this filter will converge. For both cases, the final step would be to test the application of the designed filter solutions in field experiments.

References

[1] S. A. Gafurov and E. V. Klochkov, "Autonomous Unmanned Underwater Vehicles Development Tendencies," *Procedia Engineering*, vol. 106, pp. 141–148, 2015.

[2] K. Zwolak, B. Simpson, B. Anderson, E. Bazhenova, R. Falconer, T. Kearns, H. Minami, J. Roperez, A. Rosedee, H. Sade, N. Tinmouth, R. Wigley, and Y. Zarayskaya, "An unmanned seafloor mapping system: The concept of an auv integrated with the newly designed usv sea-kit," in *OCEANS 2017 - Aberdeen*, 2017, pp. 1–6.

[3] H. Bray. (2014, Apr. 14) Bluefin robot joins search for missing malaysian plane. [Online]. Available: https://www3.bostonglobe.com/business/2014/04/14/bluefin/L9to17XsyJsxqRtoNigKkO/story.html?arc404=true

[4] A. Turetta, G. Casalino, E. Simetti, A. Sperindè, and S. Torelli, "Analysis of the accuracy of a LBL-based underwater localization procedure," *2014 Oceans - St. John's, OCEANS 2014*, 2015.

[5] S. M. Smith and D. Kronen, "Experimental results of an inexpensive short baseline acoustic positioning system for AUV navigation," *Oceans Conference Record (IEEE)*, vol. 1, pp. 714–720, 1997.

[6] J. . Peyronnet, R. Person, and F. Rybicki, "Posidonia 6000: a new long range highly accurate ultra short base line positioning system," in *IEEE Oceanic Engineering Society. OCEANS'98. Conference Proceedings (Cat. No.98CH36259)*, vol. 3, 1998, pp. 1721–1727 vol.3.

[7] J. Reis, M. Morgado, P. Batista, P. Oliveira, and C. Silvestre, "Design and experimental validation of a USBL underwater acoustic positioning system," *Sensors (Switzerland)*, vol. 16, no. 9, pp. 1–23, 2016.

[8] K. Vickery, "Acoustic positioning systems - a practical overview of current systems," pp. 5–17, 1998.

[9] M. B. Larsen, "Synthetic long baseline navigation of underwater vehicles," *Oceans Conference Record (IEEE)*, vol. 3, pp. 2043–2050, 2000.

[10] C. E. LaPointe, "Virtual long baseline ({VLBL}) autonomous underwater vehicle navigation using a single transponder," *Masterś thesis, Massachusetts Institute of Technology and Woods Hole Oceanographic Institution*, 2006.

[11] T. Casey, B. Guimond, and J. Hu, "Underwater vehicle positioning based on time of arrival measurements from a single beacon," in *OCEANS 2007*, 2007, pp. 1–8.

[12] P. Lee, B. Jun, K. Kim, J. Lee, T. Aoki, and T. Hyakudome, "Simulation of an inertial acoustic navigation system with range aiding for an autonomous underwater vehicle," *IEEE Journal of Oceanic Engineering*, vol. 32, no. 2, pp. 327–345, 2007.

[13] K. Reif, S. Günther, E. Yaz, and R. Unbehauen, "Stochastic stability of the discrete-time extended Kalman filter," *IEEE Transactions on Automatic Control*, vol. 44, no. 4, pp. 714–728, 1999.

[14] S. E. Webster, R. M. Eustice, H. Singh, and L. L. Whitcomb, "Preliminary deep water results in single-beacon one-way-travel-time acoustic navigation for underwater vehicles," *2009 IEEE/RSJ International Conference on Intelligent Robots and Systems, IROS 2009*, no. December, pp. 2053–2060, 2009.

[15] P. Batista, C. Silvestre, and P. Oliveira, "Single range aided navigation and source localization: Observability and filter design," *Systems and Control Letters*, vol. 60, no. 8, pp. 665–673, 2011.

[16] G. Indiveri, D. De Palma, and G. Parlangeli, "Single Range Localization in 3-D: Observability and Robustness Issues," *IEEE Transactions on Control Systems Technology*, vol. 24, no. 5, pp. 1853–1860, 2016.

[17] P. Batista, "Long baseline navigation with clock offset estimation and discrete-time measurements," *Control Engineering Practice*, vol. 35, pp. 43–53, 2015.

[18] ——, "Navigation and source localization based on single pseudo-ranges," *Proceedings of the American Control Conference*, vol. 2020-July, pp. 5237–5242, 2020.